RSC Advances

ROYAL SOCIETY OF CHEMISTRY

PAPER

View Article Online
View Journal | View Issue

Check for updates

Cite this: *RSC Adv.*, 2020, **10**, 22242

Enhanced capacitive performance by improving the graphitized structure in carbon aerogel microspheres†

Xichuan Liu,[ab] Lei Yuan,[a] Minglong Zhong,[a] Shuang Ni,[a] Fan Yang,[a] Zhibing Fu,[a] Xibin Xu,[a] Chaoyang Wang*[a] and Yongjian Tang*[ab]

Received 23rd February 2020
Accepted 4th June 2020

DOI: 10.1039/d0ra01735c

rsc.li/rsc-advances

Herein, good electrical conductivity and high specific surface area carbon aerogel (CA) microspheres were synthesized by a facile and economical route using a high temperature carbonization and CO_2 activation method. The electroconductive graphitized structure of the CA microspheres could be easily improved by increasing the carbonization temperature. Then the CA microspheres were activated with CO_2 to increase the specific surface area of the electrode material for electric double layer capacitors (EDLC). The sample carbonized at 1500 °C for 0.5 h and CO_2 activated at 950 °C for 8 h showed an acceptable specific surface area and excellent cycle performance and rate capability for EDLC: 98% of the initial value of the capacitance was retained after 10 000 cycles, a specific capacitance of 121 F g^{-1} at 0.2 A g^{-1} and 101 F g^{-1} at 2 A g^{-1}.

1. Introduction

With the ever-increasing demand for high performance energy storage devices, supercapacitors have been widely studied for their extremely high power density, long cycle life, and reasonable energy density.[1–3] The electric double layer capacitors (EDLC) are some of the most important supercapacitors that store energy through charge separation at the electrochemical interface between a carbon-based electrode and a liquid electrolyte. Carbon aerogels (CAs) are promising electrode materials for EDLC due to their excellent properties of interconnected three-dimensional networks, large surface area, and high electrical conductivity.[4,5] However, the complexity and high cost of preparation of the CA monolith limit their popularization.[5] To overcome this limitation, CA microspheres have drawn more attention because of their more economic preparation process[6] compared to CA monoliths.

For EDLC application, the specific surface area of the carbon electrode material is an important factor in the electrical double layer (EDL) formation. However, the low cost CA microspheres generally suffer from a low specific surface area. In order to attain high specific surface area CAs, activation methods involving chemical activation and physical activation are applied. The chemical activation process is to impregnate the raw CAs with certain chemicals (typically strong base[7,8]) prior to carbonization at lower temperatures (450–900 °C). And during the physical activation method, the as-prepared CAs is thermal treatment in the presence of an oxidizing agent such as carbon dioxide.[9–13] The main advantage of physical activation over chemical activation is that it avoids the incorporation of impurities cause by the activating agent, which is the most commonly used activation method for CAs.

Apart from specific surface area, good electrical conductivity and effective pore size distribution of carbon electrode also affect the performance of supercapacitors. Specifically, the good electrical conductivity of electrode materials will greatly affect the rate capability and cycle life of supercapacitors.[14] In order to improve the electrical conductivity of carbon-based materials, an efficient way of heteroatom doping (such as nitrogen[15–17] and phosphorusc[18]) is commonly applied. However, the heteroatom doping method always complicated the preparation procedure of CAs. Interestingly, a simple way to improve the electrical conductivity of CAs is increasing the graphitized structure in CAs,[19] which could easily achieving *via* increasing the carbonization temperature. After carbonization at high temperature and further CO_2 activation, the CAs with high specific surface area and good electrical conductivity can be expected obtained.

In this work, to address both good electrical conductivity and high specific surface area, a facile and economical synthesis route was developed to construct CA microspheres by the combination of two previous breakthroughs. On one hand, the electroconductive graphitized group is introduced by carbonizing CA microspheres at high temperature, and the CA

---

[a] *Science and Technology on Plasma Physics Laboratory, Research Centre of Laser Fusion, China Academy of Engineering Physics, Mianyang 619000, China. E-mail: wangchy807@caep.cn; tangyongjian2000@sina.com; Tel: +8608162480862; +8608162480867*

[b] *Shanghai EBIT Lab, Key Laboratory of Nuclear Physics and Ion-beam Application, Institute of Modern Physics, Department of Nuclear Science and Technology, Fudan University, Shanghai 200433, China*

† Electronic supplementary information (ESI) available. See DOI: 10.1039/d0ra01735c

Open Access Article. Published on 10 June 2020. Downloaded on 2/7/2026 10:52:31 AM.
This article is licensed under a Creative Commons Attribution-NonCommercial 3.0 Unported Licence.

This journal is © The Royal Society of Chemistry 2020

Open Access Article. Published on 10 June 2020. Downloaded on 2/7/2026 10:52:31 AM. This article is licensed under a Creative Commons Attribution-NonCommercial 3.0 Unported Licence.

microspheres with various graphitized degree are prepared at different carbonization temperatures. On the other hand, we adopt the CO_2 assisted activation method to add more quantities of micropores, and these micropores are able to provide a large surface area to form EDL and expected to exhibit high specific capacitance in EDLC. Using such graphitized CA microspheres as electrode material, supercapacitors are expected to exhibit excellent cycling stability and outstanding rate performance.

2. Experimental section

2.1 Preparation of the materials

CA microspheres were synthesized by inverse emulsion polycondensation of resorcinol (R) and formaldehyde (F), using deionized water and Na_2CO_3 as solvent and catalyst, respectively. Firstly, the RF solution was prepared by the following approach: R was dissolved in formaldehyde (molar ratios R : F = 1 : 2) and stirred for a few minutes to get clear solution; then Na_2CO_3 solution (0.02 mol L^{-1}) was mixed in the solution by molar ratios of 500 : 1 (R : Na_2CO_3), followed adding deionized water to a given volume; this solution was then stirred for about 20 minutes until light yellow RF solution was obtained. Secondly, as shown in Fig. 1, oil phase composed of 600 mL industrial white oil and 6 g surfactant span-80 were added in a three-necked flask which was soaked in a 60 °C oil bath; then the above RF solution was added drop wise to the oil phase and stirred with magnetic stirrer at 1000 rpm. Under the high-speed stirring, RF aqueous solution is dispersed in the oil phase in the shape of microspheres. The solution was stirred at 1000 rpm for 0.5 hours and continued stirred at a decelerated speed of 100 rpm for 12 hours until the dispersive RF microspheres were completely gelled. Thirdly, the gelled RF microspheres were separated from the oil phase by the filtration method and washed several times with dichloromethane, and then dried at ambient condition. Dried RF microspheres were carbonized in a tubular furnace with an argon flow rate of 100 mL min^{-1} at temperature of 1050 °C for 4 hours to obtain CAs. The graphitization treatment of CA microspheres was carried out in tubular furnace with argon atmosphere at temperature of 1500, 2000, 2500 and 2800 °C for 0.5 hours, respectively, and these graphitized CA microspheres (GCAs) are denoted as G1500, G2000, G2500, G2800, respectively. In the final CO_2 activation step, the CAs and GCAs were heated from room temperature to desired temperatures with a heating rate of 10 °C min^{-1} for a certain time under a steady CO_2 flow of 150 mL min^{-1} (Table 1).

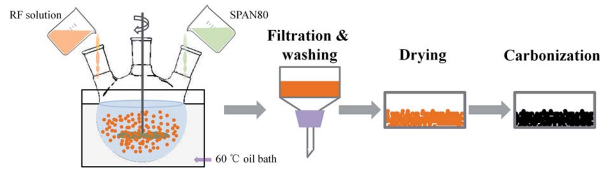

Fig. 1 Diagram of the preparation process of CA microspheres.

Table 1 The temperature and duration of CO_2 activation

Sample	CAs	G1500	G2000	G2500	G2800
Temperature (°C)	950	950	950	950	950
Time (hours)	8	8	8	8	8
Designation	CAs-8	G1500-8	G2000-8	G2500-8	G2800-8

2.2 Characterization of the samples

The microstructure of the CAs and GCAs were observed using scanning electron microscopy (SEM) and high-resolution transmission electron microscopy (HRTEM). The X-ray powder diffraction (XRD) and Raman spectroscopy (514.5 nm, Spectra Physics) were used to study the crystallographical information and phase state. The chemical composition of the CAs was analysed by X-ray photoelectron spectroscopy (XPS). N_2 adsorption and desorption isotherms were conducted with the AUTOSORB-IQ surface area analyzer at 77 K. The specific surface areas were determined on the Brunauer–Emmett–Teller (BET) method.

2.3 Theoretical calculation

Based on the density functional theory implemented in the Vienna *Ab initio* Simulation Package (VASP), calculations were carried out with employment of the Perdew, Burke, and Ernzerhof exchange-correlation functional within the generalized gradient approximation and the projector augmented-wave pseudopotential.[20] A 20.0 × 20.0 × 10.0 $Å^3$ super cell was used in this case. All geometry structures were fully relaxed until the forces on each atom are less than 0.01 eV $Å^{-1}$. Geometry optimizations and static calculations were performed with 1 × 1 × 1 *k*-point sampling.

2.4 Electrochemical measurements

Electrochemical experiments were carried out in a symmetrical sandwich-type supercapacitor. The working electrodes were fabricated as follow: the active materials (80 wt%), acetylene black (10 wt%), and polytetrafluoroethylene (10 wt%) was mixed in ethanol and ultrasonicated for 30 min; after dried at 60 °C for 24 h in vacuum, the mixture was pressed onto nickel foam under 20 MPa in round shape with a diameter of 16 mm and mass loading about 8 mg. A symmetrical supercapacitor was assembled in ambient condition after the working electrode was soaked in 6 M (mol L^{-1}) KOH solution and vacuuming for 30 min. A typical cell comprised a pair of electrodes with equal mass of active materials as both positive and negative electrode, a piece of sulfonated polypropylene membrane as separator, and 6 M KOH solution as electrolyte. Cyclic voltammetry (CV, 0–1 V) and electrochemical impedance spectroscopy (EIS, 0.01–100k Hz) measurements were performed by a CHI 760 electrochemical workstation. Rate capability and cycling performance were estimated by galvanostatic charge/discharge (GCD) tests by LAND cell test instrument, and the charge/discharge current were derived from the total mass on both two electrodes.

Open Access Article. Published on 10 June 2020. Downloaded on 2/7/2026 10:52:31 AM.
This article is licensed under a Creative Commons Attribution-NonCommercial 3.0 Unported Licence.

3. Results and discussion

3.1 Morphologies information

The morphology of the CAs and GCAs were investigated by SEM, as shown in Fig. 2 and S1.† It can be observed that the CAs is spherical in shape with diameters of 1–15 μm (Fig. 2a), possessing a smooth surface without cracks even at high magnification. Additionally, the CAs contains only carbon and oxygen without impurities as demonstrated by the XPS analysis in Fig. S2.† Even after graphitization treatment at different temperature, the morphology of GCAs is observed almost the same as that of CAs. The detailed structures of CAs and GCAs were further disclosed by HRTEM characteristics (Fig. 2 and S1†). Numerous small irregular lattice fringes can be observed for CAs (Fig. 2c), indicating the existence of graphite crystallite or disorder graphite layers in CAs. Furthermore, with the increase of graphitization temperature, the lattice fringes became more clearly and regularly.

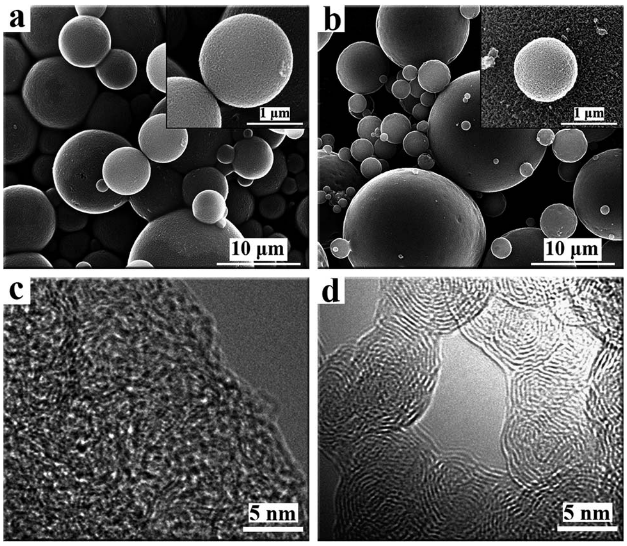

Fig. 2 SEM images (a and b) and HRTEM images (c and d) of CAs and G2800, respectively.

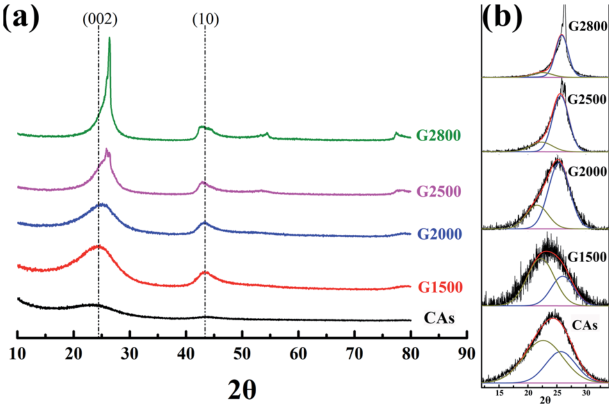

Fig. 3 XRD patterns (a) and curve-fitting of (002) peaks (b) for CAs and GCAs.

3.2 XRD analysis

XRD analysis is used to further investigate the crystalline structure of the samples. Generally, by using the Bragg and Scherrer equations,[21–24] the main characteristic peaks (002 and 100) can determine the carbon crystallite lattice parameters of interlayer spacing (d_{002}), crystallite height (L_c) and crystallite width (L_a). Where d_{002} and L_c are measured from the (002) peak with the scattering angle (2θ) at about 26° and the L_a is measured from the (100) peak with the scattering angle (2θ) at about 44°. However, the main characteristic peaks (002) of CAs and GCAs are asymmetric, as shown in Fig. 3a. It is due to the different carbon crystalline structures of CAs and GCAs. In this study, the carbon crystalline structure of CAs and GCAs are classified into a relatively good crystalline structure (G) and a pool crystalline structure (P) according to the classification by Gao *et al.*[25] The separated Gauss curves for CAs and GCAs are presented in Fig. 3b. The crystallite lattice parameters of separated components also can be calculated from the Bragg and Scherrer equations:

$$d_{002,\mathrm{G}} = \lambda/2\sin\theta_{002,\mathrm{G}} \tag{1}$$

$$d_{002,\mathrm{P}} = \lambda/2\sin\theta_{002,\mathrm{P}} \tag{2}$$

$$L_{\mathrm{c,G}} = 0.94\lambda/B_{002,\mathrm{G}}\cos\theta_{002,\mathrm{G}} \tag{3}$$

$$L_{\mathrm{c,P}} = 0.94\lambda/B_{002,\mathrm{P}}\cos\theta_{002,\mathrm{P}} \tag{4}$$

where λ is the X-ray wavelength (0.15406 nm for Cu radiation), $d_{002,\mathrm{G}}$ and $d_{002,\mathrm{C}}$ are the interlayer spacing of the separated G component and the separated P component, respectively, the $L_{\mathrm{c,G}}$ and $L_{\mathrm{c,P}}$, $B_{002,\mathrm{G}}$ and $B_{002,\mathrm{P}}$, $\theta_{002,\mathrm{G}}$ and $\theta_{002,\mathrm{P}}$ are the corresponding crystallite height, half maximum (FWHM, radians), and scattering angles (radians), respectively. Then the average crystallite lattice parameters are calculated as following equations:

$$d_{002,\mathrm{a}} = X_{\mathrm{G}}d_{002,\mathrm{G}} + X_{\mathrm{C}}d_{002,\mathrm{G}} \tag{5}$$

$$L_{\mathrm{c,a}} = X_{\mathrm{G}}L_{\mathrm{c,G}} + X_{\mathrm{P}}L_{\mathrm{c,P}} \tag{6}$$

$$X_{\mathrm{G}} = S_{\mathrm{G}}/(S_{\mathrm{G}} + S_{\mathrm{P}}) \tag{7}$$

$$X_{\mathrm{P}} = S_{\mathrm{P}}/(S_{\mathrm{G}} + S_{\mathrm{P}}) \tag{8}$$

where $d_{002,\mathrm{a}}$ and $L_{\mathrm{c,a}}$ are the average interlayer spacing and the average crystallite height, respectively, X_{G} and X_{P} are the fractions of the G component and the P component, respectively, and the S_{G} and S_{P} are the corresponding areas.

The calculated values of all parameters for CAs and GCAs are presented in Table 2. As shown in Fig. 3a, the (002) peak becomes sharper with the increase of graphitized temperature, which indicates that the crystallinity of GCAs is apparently improved. In addition, the position of (002) peak shifts to the high scattering angles while the (10) peak shifts to the low scattering angles along with the rise of graphitized treatment temperature, which implicates the more compact interlayer

Open Access Article. Published on 10 June 2020. Downloaded on 2/7/2026 10:52:31 AM.
This article is licensed under a Creative Commons Attribution-NonCommercial 3.0 Unported Licence.

Table 2 The XRD structure parameters of CAs and GCAs

Sample	$d_{002,G}$ (nm)	$d_{002,P}$ (nm)	$L_{c,G}$ (nm)	$L_{c,P}$ (nm)	X_G	X_P	$d_{002,a}$[a] (nm)	$L_{c,a}$[b] (nm)	L_a[c] (nm)
CAs	0.400	0.342	1.524	1.821	0.35	0.65	0.380	1.543	4.272
G1500	0.352	0.417	1.597	1.450	0.38	0.62	0.376	1.627	4.389
G2000	0.351	0.411	1.976	1.903	0.73	0.27	0.367	1.956	5.270
G2500	0.347	0.398	2.585	1.889	0.81	0.19	0.357	2.453	6.571
G2800	0.345	0.407	3.062	2.200	0.87	0.13	0.353	2.950	7.599

[a] $d_{002,a}$: average interlayer spacing. [b] $L_{c,a}$: average crystallite height. [c] L_a: crystallite width.

spacing and the increase of crystallite width of GCAs crystal structure.[26] These results are agreement with the calculated crystallite lattice parameters shown in Table 2, while the graphitized treatment temperature increases to 2800 °C, the $d_{002,a}$ decreases to 0.353 nm, the $L_{c,a}$ increases to 2.950 nm and the L_a increases to 7.599 nm, respectively. These parameters clearly display the crystal growth process in CAs and GCAs.

3.3 Raman spectroscope and spectral analysis

To further examine the structure differences of the various graphitized CAs, Raman spectroscopy were measured and shown in Fig. 4. The Raman spectra show two main bands located at about 1350 cm^{-1} and 1600 cm^{-1}. Each spectrum can be resolved into 4 Lorentzian bands (around 1200, 1350, 1580, and 1620 cm^{-1}) and 1 Gaussian band (around 1530 cm^{-1}).[27,28] The G band around 1580 cm^{-1} corresponds to an ideal graphitic lattice aromatic vibration mode with E_{2g} symmetry. The appearance of band around 1350 cm^{-1} is commonly called D1 band, which is assigned to a graphitic lattice vibration mode with A_{1g} symmetry.[29,30] The D1 band has been suggested to arise from graphene layer carbon atoms in immediate vicinity of a lattice disturbance like the edge of a graphene layer.[27,30–32] The band around 1620 cm^{-1} is called D2 band, corresponding to a graphitic lattice mode with E_{2g} symmetry and involving graphene layers at the surface of a graphitic crystal.[27,33] The relative intensities of both the D1 and D2 bands could be used to characterize the degree of disorder in the graphitic structure.[34,35] The band at around 1530 cm^{-1} has been assumed Gaussian line shape and designated D3 band.[27,36] This D3 band is originated from the amorphous carbon fraction of carbonaceous materials.[28,36] The peak at D1 band exhibits a shoulder at around 1200 cm^{-1}, which has been denominated as D4 band. Dippel *et al.* tentatively attribute D4 band to sp^2–sp^3 mixed sites at the periphery of crystallites or to C–C and C=C stretching vibrations of polyene-like structures.[37,38]

Transformations of Raman spectra as a function of the graphitized-treatment temperature are displayed in Fig. 4. The band area ratios of the defect bands to the G band (appropriately denoted as I_{D1}/I_G, I_{D2}/I_G, I_{D3}/I_G and I_{D4}/I_G) and the additional ratio of the G band to the integrated area under the spectrum (I_G/I_{All}) are presented in Table 3 for comparison. During graphitization-treatment, the relative intensities (ratios of band areas) and FWHM of band were significantly changed

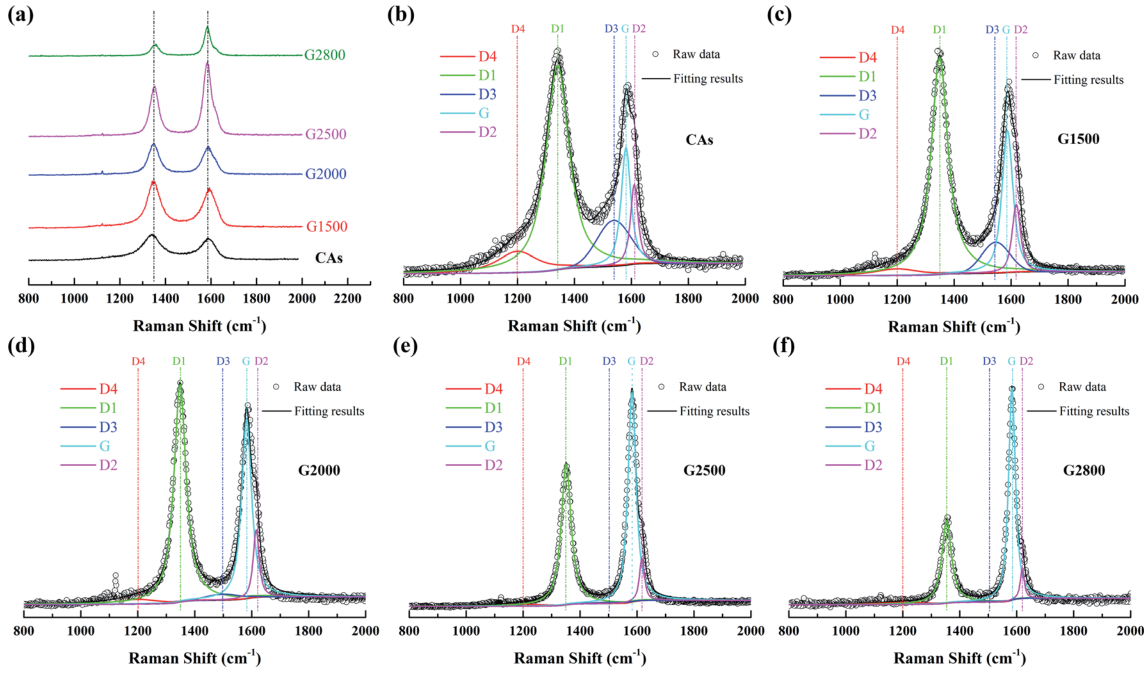

Fig. 4 First-order Raman spectrum (a) and the relative fitting curve of CAs (b), G1500 (c), G2000 (d), G2500 (e), and G2800 (f).

Open Access Article. Published on 10 June 2020. Downloaded on 2/7/2026 10:52:31 AM.
This article is licensed under a Creative Commons Attribution-NonCommercial 3.0 Unported Licence.

Table 3 The curve-fitted Raman spectra parameters of CAs and GCAs

Sample	I_{D1}/I_G	I_{D2}/I_G	I_{D3}/I_G	I_{D4}/I_G	I_G/I_{All}
CAs	4.250	0.536	0.972	0.756	0.133
G1500	2.539	0.356	0.403	0.198	0.222
G2000	1.550	0.223	0.080	0.112	0.337
G2500	0.859	0.124	—	—	0.504
G2800	0.558	0.080	—	—	0.611

while their positions almost invariable. Obviously, the intensity (band area) of G band and D1 band varies in the opposite direction, while the two bands become narrower. Such FWHM decreases of D1 band and G band are related to the degree of ordered graphitic structure. Miroslawa Pawlyta *et al.* found that the Raman-based classification matches well with HRTEM observations: with growing larger of the layers directly imaged by HRTEM image, the G-band becomes sharper.[39] Our results are in good agreement with this relationship. In addition, intensities of the D3 band and the D4 band are gradually decrease with the increase of graphitized treatment temperature, and these bands can be neglected for samples heated above 2000 °C. Specifically, the D2 band remains distinct from the G band although its area ratio to the G band is also gradually decreased. As shown in the Table 3, that I_{D1}/I_G, I_{D2}/I_G, I_{D3}/I_G and I_{D4}/I_G decrease significantly, while I_G/I_{All} increases significantly with the increase of the graphitic treatment temperature. The decrease of these band ratios means that various crystal defects in CAs are gradually eliminated. In fact, the descend of I_{D1}/I_G means that the average plane size of graphitic crystallites increases.[40] And the decrease of I_{D2}/I_G indicates the decrease of the surface to volume ratio of graphitic crystals, namely the growth of graphitic crystals.[33] While the decrease of I_{D3}/I_G and I_{D4}/I_G means the amorphous carbon transforms into crystalline form. Consequently, more ordered graphitic structure is formed with the increased graphitic treatment temperatures, which lead to the increase of I_G/I_{All}.[28]

3.4 Porous properties

From the above analysis, the CA microspheres with various graphitized structure have been successfully prepared which are then treated with CO_2 activation to improve their surface area. The nitrogen adsorption/desorption isotherms are used to characterize the pore properties of the CAs, GCAs (shown in Fig. 5a) and activated samples (shown in Fig. 5b). And the corresponding pore parameters of BET surface area (S_{BET}) and total pore volume (V_t) are displayed in Table S1.†

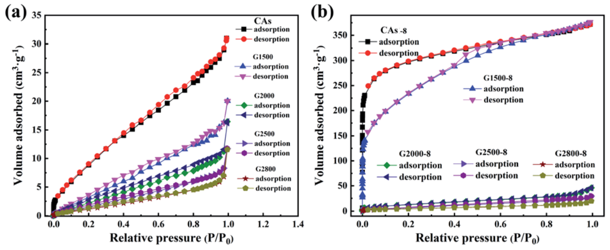

Fig. 5 Nitrogen adsorption/desorption isotherms of the CAs, GCAs (a) and according activated samples (b).

It can be seen from Table S1† that the BET specific surface area of CAs is 42.9 $m^2 g^{-1}$ and decreases with the increase of graphitization temperature. While adopting the CO_2 activation, the corresponding BET specific surface area of both CAs and G1500 are greatly increased (Table S1†), but the G2000-8, G2500-8 and G2800-8 are slightly increased. This is attributed to the different reactivity with CO_2 of carbon atoms at edge of graphite layer and those interior atoms. Previous studies suggest that the edge structures of carbon basal plane are identified as active sites for the gasification reaction.[41–43] With the increased carbonization temperature, the increased graphitized group results in the decrease of carbon atoms at edge of graphite layer act as active sites. Furthermore, our theoretical calculation results also show that the energy required etching a carbon atom from the inside of the graphite layer (Fig. S3†) is about 7.25 eV higher than that required from the edge. In addition, the CAs-8 and G1500-8 exhibit the most increased BET specific surface area (S_{BET}) of 1107 and 715 $m^2 g^{-1}$ (Table S1†), and the corresponding pore parameters and pore size distribution are summarized in Table 4 and Fig. S4,† respectively. As shown in Table 4 and Fig. S4,† CAs-8 exhibit a large micropores surface area (S_{mic}) of 953 $m^2 g^{-1}$ (86% of S_{BET}), implying that the CO_2 activation is directly accountable for micropores formation (pore size < 2 nm).[44] In contrast, the G1500-8 shows a smaller S_{mic} proportion (64% of S_{BET}) and more mesopores (2 < pore size < 50 nm) distribution than CAs-8. The results suggest that more mesopores are tends to produced by CO_2 activation in G1500.

3.5 Electrochemical performance

The GCD curves of CAs, CAs-8, G1500, and G1500-8 electrodes are shown in Fig. 6a, and the single-electrode specific capacitance C_s is evaluated base on following equation,[45]

$$C_s = \frac{2I\Delta t}{m\Delta U} \tag{9}$$

where I is the conducted current, m is the mass of the active materials on one electrode, Δt and ΔU is the discharge-time and the potential difference during the discharge process after the internal resistance (IR) drop. The IR drop is generally associated with the equivalent series resistance (ESR), and the ESR is the sum of resistances including the electronic resistance of electrode, the ions diffusing resistance in the nanopores of electrode materials, and the interfacial resistance between the electrode and the current collector.[46,47] The specific capacitances of CAs and G1500 calculated from the discharge curve are 12 and 5.6 F g^{-1} at current density of 0.2 A g^{-1}, respectively. After CO_2 activation, the specific capacitances of CAs-8 and G1500-8 are significantly increased to 115 and 121 F g^{-1}, respectively. Remarkably, the CAs-8 with larger specific surface area (1107 $m^2 g^{-1}$) than G1500-8 (715 $m^2 g^{-1}$) (Table 4) exhibits the lower specific capacitance. This capacitance difference

Open Access Article. Published on 10 June 2020. Downloaded on 2/7/2026 10:52:31 AM.
This article is licensed under a Creative Commons Attribution-NonCommercial 3.0 Unported Licence.

Table 4 Corresponding pore parameters of the CAs-8 and G1500-8

Sample	S_{BET}[a]/(m^2 g^{-1})	S_{mic}[b]/(m^2 g^{-1})	S_{ext}[c]/(m^2 g^{-1})	V_t[d]/(cm^3 g^{-1})	V_{mic}[e]/(cm^3 g^{-1})	A_p[f] (nm)
CAs	42.9	0	42.9	0.047	0	4.5
CAs-8	1107	953	154	0.575	0.406	2.1
G1500	22.3	0	22.3	0.039	0	5.6
G1500-8	715	464	251	0.484	0.237	2.7

[a] S_{BET}: BET surface area. [b] S_{mic}: micropores surface area. [c] S_{ext}: external surface area including mesopores and macropores. [d] V_t: total pore volume. [e] V_{mic}: micropore volume. [f] A_p: average pore diameter.

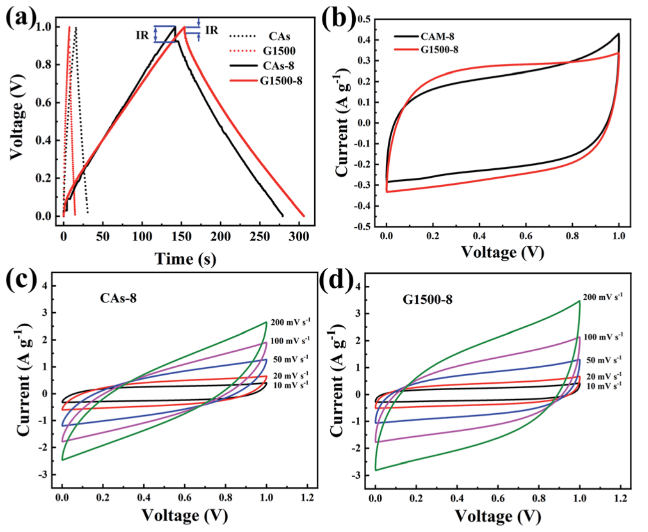

Fig. 6 The GCD curves of CAs, CAs-8, G1500, and G1500-8 electrodes at 0.2 A g^{-1} (a) CV curves of the CAs-8 and G1500-8 at scan rate of 10 mV s^{-1} (b) the CV curves at different scan rates of CAs-8 (c) and G1500-8 (d) electrodes.

could be attributed to the CAs-8 possess higher micropores content than G1500-8, this high micropores levels cause the harder transportation of electrolyte ions to whole inner surface. In addition, the GCD curves of G2000-8, G2500-8 and G2800-8 at 0.05 A g^{-1} are shown in Fig. S5.† From the above analysis, it is difficult to improve the specific surface area of G2000, G2500 and G2800 by CO$_2$ activation, resulting in the extremely low specific surface area (Table S1†). And the specific capacitance of G2000-8, G2500-8 and G2800-8 are calculated to be only 12.6, 7.2 and 3 F g^{-1} even at a low current density of 0.05 A g^{-1}, respectively. Therefore, the electrochemical properties of CAs-8 and G1500-8 are mainly compared in following section.

Fig. 6b shows the CV profiles CAs-8 and G1500-8 at a scan rate of 10 mV s^{-1} in a potential window range of 0–1 V. It is known that a good electrode material for EDLC should be capable of providing very fast electrolyte ion transport pathways, resulting in a rectangular-shaped CV curve.[48,49] Hence, the rectangle degree of CV profile can reflect the electrolyte ion diffusion rate within a carbon nanostructure. As show in Fig. 6b, the CV profiles of G1500-8 display a higher rectangle degree than CAs-8, indicating the faster ion diffusion rate of G1500-8 than CAs-8. Furthermore, as show in Fig. 6c and d, the CV curves of CAs-8 display a more severe distortion than G1500-8 at different scan rates. The high rectangle degree and moderately distortion at different scan rates of G1500 electrode is attributed to following factors: (a) the graphitized group can improve its intrinsic conductivity; (b) the mesoporous structure shortens the ion-diffusion route.

Fig. 7a and b shows the performance of the CAs-8 and G1500-8, respectively. After 10 000 cycles, the specific capacitance retention of CAs-8 and G1500-8 is 98% and 92%, respectively. Fig. 7c shows the specific capacitance of CAs-8 and G1500-8 at different current density, and the specific capacitance at 2 A g^{-1} remains 61% and 84% of the value at 0.2 A g^{-1} for CAs-8 and G1500-8, respectively. The excellent rate capability and long cycle life of G1500-8 is also suggested by that: (a) the more graphitized group can improve its intrinsic conductivity; and (b) the more mesoporous structure shortens the ion-diffusion route and increases the effective surface area for EDL. Fig. 7d shows the Nyquist plot of the CAs-8 and G1500-8 electrode, and the Nyquist plot can be fitted by the electrical equivalent circuit shown in the figure inset. Generally, the R_b is the combinational resistance of the ionic resistance of the electrolyte, the intrinsic resistance of active materials, and the contact resistance at the active materials/current collector interface; the R_{CT} is the charge-transfer resistance; the CPE1 is double-layer capacitance; Z_W is the Warburg impedance; and the CPE2 is the limiting capacitance.[11,45,50,51] It is found that the R_b of CAs-8 and

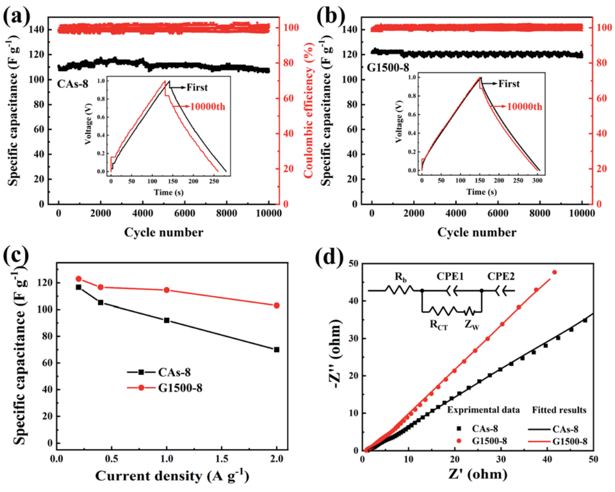

Fig. 7 The cycle performance of the CAs-8 (a) and G1500-8 (b) at the current density of 0.2 A g^{-1}; the rate capability (c), Nyquist plots (d) and equivalent circuit (inset) of CAs-8 and G1500-8, respectively.

Open Access Article. Published on 10 June 2020. Downloaded on 2/7/2026 10:52:31 AM. This article is licensed under a Creative Commons Attribution-NonCommercial 3.0 Unported Licence.

G1500-8 is 0.88 and 0.79 Ω, respectively. The lower R_b of G1500-8 is attributed to the higher intrinsic conductivity caused by the more graphite group. Moreover, the R_{CT} of CAs-8 and G1500-8 is 0.26 and 0.15 Ω, respectively, clearly, the more mesoporous structure of G1500-8 shortens the ion-diffusion route resulting in the lower R_{CT}. The sum of R_b and R_{CT} is the main contributor to ESR, which limits the charging/discharging rate of the SCs.[45] Furthermore, the higher Warburg angle of G1500-8 than CAs-8 indicates the better ion diffusion performance and capacitive performance of G1500-8. As a results, the G1500-8 with more graphite group and mesoporous structure exhibit the enhanced capacitive performance in EDLC.

Finally, we note that the specific surface area of G2000, G2500 and G2800 is hard to improve by CO_2 activation for their excessive graphitized group, but the structure of G1500-8 could be significantly improved by CO_2 activation. Furthermore, besides the high specific area, the G1500-8 exhibits a high proportion of mesoporous structure. This result is attributed to the moderate content of graphitized group in G1500, which not only improve its intrinsic conductivity but also provide fewer gasification reactive sites during CO_2 activation, resulting in the formation of mesopores. These properties are the critical factor of improvements in all electrochemical properties when these CA microspheres are used as electrode of EDLC. However, the extremely low specific surface area of raw CA microspheres limits the further enhancement of G1500-8 performance. As such, the development of modified methods for CA microspheres with high initial surface area and moderate graphitized group formation should be intensified.

4. Conclusions

To summary, our incorporating considerations both increasing graphitized structure and CO_2 activation are proved to obtain CAs microsphere with improved electoral conductivity and high surface area. The sample G1500-8 carbonized at 1500 °C for 0.5 h and CO_2 activated at 950 °C for 8 h exhibit the acceptable specific surface area of 715 $m^2\ g^{-1}$ and the excellent cycle performance and rate capability for EDLC: 98% capacitance retain of initial value after 10 000 cycles, specific capacitance of 121 F g^{-1} at 0.2 A g^{-1} and 101 F g^{-1} even at 2 A g^{-1}. Although, the increasing graphitized structure method cannot be used excessively to create electroconductive group to improve the electrical conductivity of CAs, which is an important and facile route to improve the electrochemical performance of carbon electrode materials for EDLC.

Conflicts of interest

There are no conflicts to declare.

Acknowledgements

This work is supported by the National Natural Science Foundation of China (grant no: 11604311). We gratefully appreciated our co-workers for their valuable discussions and assistance in measurements. We are grateful to Qingjun, Zhang, Shufan Chen, Qi Yang, Yong Zeng, and Jia Li (Science and Technology on plasma physics Laboratory, Research Centre of Laser Fusion, China Academy of Engineering physics, Mianyang, China) for their assistance in measurements.

Notes and references

1 Y. Wang, Y. Song and Y. Xia, *Chem. Soc. Rev.*, 2016, **45**, 5925–5950.
2 J. Jia, X. Liu, R. Mi, N. Liu, Z. Xiong, L. Yuan, C. Wang, G. Sheng, L. Cao and X. Zhou, *J. Mater. Chem. A*, 2018, **6**, 15330–15339.
3 X. Liu, G. Sheng, M. Zhong and X. Zhou, *Mater Design*, 2018, **141**, 220–229.
4 A. Allahbakhsh and A. R. Bahramian, *Nanoscale*, 2015, **7**, 14139–14158.
5 F. Li, L. Xie, G. Sun, Q. Kong, F. Su, Y. Cao, J. Wei, A. Ahmad, X. Guo and C.-M. Chen, *Micropor Mesopor Mat*, 2019, **279**, 293–315.
6 X. Quan, Z. Fu, L. Yuan, M. Zhong, R. Mi, X. Yang, Y. Yi and C. Wang, *RSC Adv.*, 2017, **7**, 35875–35882.
7 X. Zeng, D. Wu, R. Fu, H. Lai and J. Fu, *Electrochim. Acta*, 2008, **53**, 5711–5715.
8 J. Wang, X. Yang, D. Wu, R. Fu, M. S. Dresselhaus and G. Dresselhaus, *J. Power Sources*, 2008, **185**, 589–594.
9 I. Yang, D. Kwon, M.-S. Kim and J. C. Jung, *Carbon*, 2018, **132**, 503–511.
10 S. K. Ling, H. Y. Tian, S. Wang, T. Rufford, Z. H. Zhu and C. E. Buckley, *J. Colloid Interface Sci.*, 2011, **357**, 157–162.
11 Y.-M. Chang, C.-Y. Wu and P.-W. Wu, *J. Power Sources*, 2013, **223**, 147–154.
12 X. Liu, R. Mi, L. Yuan, F. Yang, Z. Fu, C. Wang and Y. Tang, *Front Chem*, 2018, **6**, 475.
13 N. Liu, J. Shen and D. Liu, *Micropor Mesopor Mat*, 2013, **167**, 176–181.
14 X. Liu, S. Li, R. Mi, J. Mei, L.-M. Liu, L. Cao, W.-M. Lau and H. Liu, *Appl Energ*, 2015, **153**, 32–40.
15 R. Liu, X. Xi, X. Xing and D. Wu, *RSC Adv.*, 2016, **6**, 83613–83618.
16 L. Wang, H. Liu, J. Zhao, X. Zhang, C. Zhang, G. Zhang, Q. Liu and H. Duan, *Chem. Eng. J.*, 2020, **382**, 122979.
17 Y. Tong, D. Ji, P. Wang, H. Zhou, K. Akhtar, X. Shen, J. Zhang and A. Yuan, *RSC Adv.*, 2017, **7**, 25182–25190.
18 X. Yan, Y. Liu, X. Fan, X. Jia, Y. Yu and X. Yang, *J. Power Sources*, 2014, **248**, 745–751.
19 W. C. Li, C. L. Mak, C. W. Kan and C. Y. Hui, *RSC Adv.*, 2014, **4**, 64890–64900.
20 S. Ni, W. He, Z. Li and J. Yang, *J. Phys. Chem. C*, 2011, **115**, 12760–12762.
21 G. A. Zickler, B. Smarsly, N. Gierlinger, H. Peterlik and O. Paris, *Carbon*, 2006, **44**, 3239–3246.
22 S. Zuo, J. Liu, J. Yang and X. Cai, *Carbon*, 2009, **47**, 3578–3580.
23 F. C. Tai, C. Wei, S. H. Chang and W. S. Chen, *J. Raman Spectrosc.*, 2010, **41**, 933–937.
24 C. Cen, Y. Zhang, X. Chen, H. Yang, Z. Yi, W. Yao, Y. Tang, Y. Yi, J. Wang and P. Wu, *Phys. E*, 2020, **117**, 113840–113852.

This journal is © The Royal Society of Chemistry 2020

Open Access Article. Published on 10 June 2020. Downloaded on 2/7/2026 10:52:31 AM.
This article is licensed under a Creative Commons Attribution-NonCommercial 3.0 Unported Licence.

25 S. Wu, J. Gu, X. Zhang, Y. Wu and J. Gao, *Energ Fuel*, 2008, **22**, 199–206.

26 L. Lu, V. Sahajwalla, C. Kong and D. Harris, *Carbon*, 2001, **39**, 1821–1833.

27 A. Sadezky, H. Muckenhuber, H. Grothe, R. Niessner and U. Pöschl, *Carbon*, 2005, **43**, 1731–1742.

28 C. Sheng, *Fuel*, 2007, **86**, 2316–2324.

29 A. C. Ferrari and J. Robertson, *Phys. Rev. B*, 2000, **61**, 14095–14107.

30 Y. Wang, D. C. Alsmeyer and R. L. McCreery, *Chem. Mater.*, 1990, **2**, 557–563.

31 G. Katagiri, H. Ishida and A. Ishitani, *Carbon*, 1988, **26**, 565–571.

32 C. Cen, Z. Chen, D. Xu, L. Jiang, X. Chen, Z. Yi, P. Wu, G. Li and Y. Yi, *Nanomaterials*, 2020, **10**, 1–12.

33 S. Sze, *Atmos. Environ.*, 2001, **35**, 561–568.

34 A. Yoshida, Y. Kaburagi and Y. Hishiyama, *Carbon*, 2006, **44**, 2333–2335.

35 O. Beyssac, B. Goffé, J.-P. Petitet, E. Froigneux, M. Moreau and J.-N. Rouzaud, *Spectrochim. Acta, Part A*, 2003, **59**, 2267–2276.

36 T. Jawhari, A. Roid and J. Casado, *Carbon*, 1995, **33**, 1561–1565.

37 B. Dippel and J. Heintzenberg, *J. Aerosol Sci.*, 1999, **30**, S907–S908.

38 B. Dippel, H. Jander and J. Heintzenberg, *Phys. Chem. Chem. Phys.*, 1999, **1**, 4707–4712.

39 M. Pawlyta, J.-N. Rouzaud and S. Duber, *Carbon*, 2015, **84**, 479–490.

40 F. Tuinstra and J. L. Koenig, *J. Chem. Phys.*, 1970, **53**, 1126–1130.

41 J. F. Strange and P. L. Walker, *Carbon*, 1976, **14**, 345–350.

42 F. Vallejos-Burgos, N. Díaz-Pérez, Á. Silva-Villalobos, R. Jiménez, X. García and L. R. Radovic, *Carbon*, 2016, **109**, 253–263.

43 P. Ehrburger, F. Louys and J. Lahaye, *Carbon*, 1989, **27**, 389–393.

44 X. Liu, S. Li, J. Mei, W.-M. Lau, R. Mi, Y. Li, H. Liu and L. Liu, *J. Mater. Chem. A*, 2014, **2**, 14429–14438.

45 J. Zhang and X. S. Zhao, *ChemSusChem*, 2012, **5**, 818–841.

46 Z. Lei, N. Christov and X. S. Zhao, *Energy Environ. Sci.*, 2011, **4**, 1866–1873.

47 C. Zhong, Y. Deng, W. Hu, J. Qiao, L. Zhang and J. Zhang, *Chem. Soc. Rev.*, 2015, **44**, 7484–7539.

48 A. Ghosh and Y. H. Lee, *ChemSusChem*, 2012, **5**, 480–499.

49 E. Frackowiak and F. Béguin, *Carbon*, 2001, **39**, 937–950.

50 D. Liu, J. Shen, N. Liu, H. Yang and A. Du, *Electrochim. Acta*, 2013, **89**, 571–576.

51 D. Liu, G. Cheng, H. Zhao, C. Zeng, D. Qu, L. Xiao, H. Tang, Z. Deng, Y. Li and B.-L. Su, *Nano Energy*, 2016, **22**, 255–268.